Order reconstruction patterns in nematic liquid crystal wells

Samo Kralj [*], Apala Majumdar* [†]

January 21, 2014

Abstract

We numerically study structural transitions inside shallow nanoscale wells with square cross-section, filled with nematic liquid crystal material. We model the wells within the Landau-de Gennes theory for nematic liquid crystals, in the absence of any external fields. We obtain two qualitatively different states: (i) the DSD state for relatively large wells with lateral dimension greater than a numerically computed critical threshold and (ii) a novel, two-dimensional star-like biaxial order reconstruction (OR) pattern called the WORS pattern, for wells smaller than the critical threshold. We define quantitative criteria for the onset of the WORS pattern in terms of the biaxiality parameter. We systematically study the dependence of the critical threshold, for the appearance of the WORS pattern, on the temperature and the anchoring strength on the lateral well surfaces.

1 Introduction

Liquid crystals (LCs) are mesogenic phases of matter with physical properties intermediate between those of the conventional solid and liquid phases of matter [2]. Nematic LCs are the simplest type of LCs; nematics are complex anisotropic liquids with a certain degree of long-range orientational ordering. The structural properties of a nematic LC can be easily manipulated by incident light, electric or magnetic fields and mechanical effects [3]. As a consequence, they exhibit a wealth of diverse physical phenomena and are often used as a testing ground for fundamental physics in condensed matter systems [12]. Nematic LCs now have widespread applications across science and technology e.g. electro-optic devices, sensors and notably, the huge and thriving liquid crystal display (LCD) industry around the globe [19, 21, 8].

*Department of Physics, Faculty of Natural Sciences and Mathematics, University of Maribor, Koroška cesta 160, SI-2000 Maribor, Slovenia and Jožef Stefan Institute, P.O. Box 3000, SI-1000 Ljubljana, Slovenia

†Department of Mathematical Sciences, University of Bath, Bath, BA2 7AY, United Kingdom

Nematics in confinement have generated tremendous interest in recent years [4, 5, 9, 3]. Such confined LC systems typically exhibit topological defects or localized material imperfections [7, 19]. Defect core structures are poorly understood; experimental and numerical studies indicate that defect cores can be associated with uniaxial-biaxial structural transitions or equivalently order reconstruction (OR) phenomena wherein the system mediates between two different uniaxial states via a continuum of biaxial states [3, 9]. OR phenomena were first reported in the benchmark paper [9]. In [9], the authors numerically analyze the interior of a defect core; the nematic LC is in a uniaxial phase at the defect centre and in a uniaxial phase away from the defect core. The corresponding directors (see (2)) are perpendicular to one another and the LC material mediates between the two conflicting uniaxial states via a continuum of biaxial states. OR phenomena were subsequently reported in a batch of numerical papers [6, 18, 13, 14] which indicate that OR phenomena typically occur in severely confined systems with comparable material and geometrical length scales or/and under the action of intense electric fields. For example, in [10], the authors study OR phenomena for a twisted hybrid nematic cell. The authors numerically find two classes of solutions: (i) the conventional purely uniaxial twisted solution wherein the molecules twist uniformly between the two boundary plates and (ii) the OR untwisted solution characterized by a biaxial band around the centre of the cell. The OR solution is the only observable solution in nano-confined geometries where the cell gap is comparable to a material-dependent length scale, known as the biaxial correlation length [6]. Experimental studies of the OR phenomenon have been reported in for e.g. [18, 24] and such studies are particularly relevant for new LC systems with intrinsic biaxiality and their potential applications in nano-science and technology.

Our work is motivated in part by the results in [20, 21] with a view to characterize novel two-dimensional (2D) OR patterns in prototype geometries. This is an interesting problem since classical OR patterns are typically one-dimensional (1D) with the structural characteristics varying along one coordinate direction, e.g. along the radial direction in a spherical droplet (see [9], along the vertical direction in a cylinder [13, 14] or along the normal direction to parallel bounding plates [10] etc. and 2D OR patterns offer new scientific possibilities. In [20, 21], the authors study a model liquid crystal device comprising a periodic array of shallow micron-sized square wells. These square wells are filled with nematic LC; the surfaces are treated so as to induce tangential or planar boundary conditions [8, 21] i.e. on the well surfaces, the LC molecules are constrained to be in the plane of the surfaces. This relatively simple geometry is bistable or multistable in the sense that there are multiple stable LC textures with contrasting optical properties [20]. In [20, 21], the authors work within the powerful Landau-de Gennes theory for nematic LCs [12]. Given that the wells are shallow, they argue that it suffices to model 2D structural variations within the plane of

the square and work with a strictly 2D model i.e. study 2D configurations on the square. They work in the macroscopic limit, where the square size, denoted by R, is on the micron-scale i.e. is much greater than the biaxial correlation length, which is typically on the nanometer scale (see [18, 6]). In this macroscopic limit, the stable LC states are effectively uniaxial almost everywhere, except for small localized defects around the square vertices [21]. The authors find two stable LC states: (i) the diagonal state with the average uniaxial alignment along one of the square diagonals and (ii) the rotated state where the average direction of alignment rotates by 180 degrees between a pair of opposite square edges.

We carefully examine the effects of nano-confinement on the same model system. In particular, we work with a three-dimensional (3D) model, under the assumption that all structural details are independent of the vertical coordinate. Our 3D modelling captures biaxiality, which is outside the scope of the 2D model employed in [20, 21]. We denote the lateral square well size by R, which is measured in terms of the biaxial correlation length, and obtain two qualitatively different LC textures as a function of R: (i) the Diagonal Structure with Defects (DSD) for "large" R and (ii) the Well Order Reconstruction Structure (WORS) for small R. The DSD is qualitatively similar to the diagonal solution in [20, 21] and our modelling reveals the biaxial nature of the defect cores around the square vertices. The WORS is a new 2D OR pattern connecting the four square vertices, characterized by a star-shaped rim of maximal biaxiality that separates a uniaxial state in the interior of the rim from a different uniaxial state outside the rim. In other words, the system mediates between two different uniaxial states via a 2D star-shaped ring of intermediate biaxial states. The WORS pattern is the only stable LC pattern for "small" wells, with R less than a critical threshold length, denoted by R_c. In Section 4, we systematically investigate how R_c depends on temperature and anchoring strength on the boundaries, to obtain quantitative information about the stability of the WORS pattern.

The paper is organized as follows. In Section II, we review the Landau-de Gennes theory for nematic LCs. In Section III, we outline the geometry of the problem, the relevant parameterizations, the material length-scales and the governing Euler-Lagrange equations. In Section IV, we present our numerical results and summarize our conclusions and future outlook in Section V.

2 Theoretical background

Let $\mathcal{B} \subset \mathbb{R}^3$ denote an arbitrary three-dimensional domain filled with nematic LC material, with a sufficiently regular boundary, $\partial\mathcal{B}$. We work within the Landau-de Gennes (LdG) theory for nematic LCs wherein the state of the nematic LC is described by a macroscopic order parameter, the $\mathbf{Q}$-tensor

parameter [2, 12]. The **Q**-tensor order parameter can be viewed as a macroscopic measure of the system anisotropy i.e. a measure of the anisotropy in dielectric response to electric fields or anisotropy in magnetic susceptibility or response to magnetic fields. Mathematically, **Q** is a symmetric, traceless 3×3 matrix and from the spectral decomposition theorem, the **Q**-tensor can be written in terms of its eigenvalues $\{s_i\}$, and eigenvectors, $\{\overrightarrow{e}_i\}$, as shown below [3]

$$\mathbf{Q} = \sum_{i=1}^{3} s_i \overrightarrow{e}_i \otimes \overrightarrow{e}_i \,. \tag{1}$$

The eigenvectors represent the distinguished directions of LC alignment and the eigenvalues are a measure of the degree of orientational ordering about these directions. A LC phase is said to be in the (i) disordered or isotropic phase if $\mathbf{Q} = 0$, (ii) uniaxial phase if **Q** has a pair of degenerate non-zero eigenvalues and (iii) the biaxial phase if **Q** has three distinct eigenvalues [12]. In the uniaxial case, **Q** can be concisely expressed as

$$\mathbf{Q} = S\left(\overrightarrow{e}_1 \otimes \overrightarrow{e}_1 - \frac{1}{3}\mathbf{I}\right), \tag{2}$$

in terms of the single distinguished eigendirection, the *director field* $\overrightarrow{e}_1$, and the scalar order parameter S. In other words, $\overrightarrow{e}_1$, is the eigenvector with the non-degenerate eigenvalue and all directions perpendicular to $\overrightarrow{e}_1$ are physically equivalent. In the biaxial phase, **Q** can be written as

$$\mathbf{Q} = S\left(\overrightarrow{e}_1 \otimes \overrightarrow{e}_1 - \frac{1}{3}\mathbf{I}\right) + R\left(\overrightarrow{e}_2 \otimes \overrightarrow{e}_2 - \overrightarrow{e}_3 \otimes \overrightarrow{e}_3\right), \tag{3}$$

where $\{\overrightarrow{e}_i\}$ are the eigenvectors and (S, R) are two scalar order parameters that measure the degree of orientational ordering about the different eigenvectors [22]. A quantitative measure of the degree of biaxiality is defined to be

$$\beta^2 = 1 - \frac{6(tr\mathbf{Q}^3)^2}{(tr\mathbf{Q}^2)^3}, \tag{4}$$

$\beta^2 \in [0, 1]$ and $\beta^2 = 0$ for all uniaxial states [8] . The maximal value, $\beta^2 = 1$, is attained if and only if one of the eigenvalues, s_i, vanishes.

The LdG theory is a variational theory and the stable physically observable LC states correspond to minimizers of an appropriately defined LdG energy functional [22]. We work with the following LdG free energy

$$F = \int_{\mathcal{B}} (f_c + f_e)\, d^3\overrightarrow{r} + \sum_i \int_{\partial\mathcal{B}} f_s^i d^2\overrightarrow{r}, \tag{5}$$

where $d^3\overrightarrow{r}$ and $d^2\overrightarrow{r}$ denote the volume and area measures, respectively [3, 23]. The condensation (f_c), elastic (f_e), and surface (f_s) free energy

densities are given by [3]

$$f_c = \frac{A_0(T-T_*)}{2} tr\mathbf{Q}^2 - \frac{B}{3} tr\mathbf{Q}^3 + \frac{C}{4}(tr\mathbf{Q}^2)^2, \quad (6)$$

$$f_e = \frac{L}{2}|\nabla \mathbf{Q}|^2, \quad (7)$$

$$f_s^{(i)} = \frac{w^{(i)}}{2} Tr\left(\mathbf{Q} - \mathbf{Q}_s^{(i)}\right)^2. \quad (8)$$

In particular, there are no external fields in this variational problem. The condensation energy dictates the preferred degree of orientational order in the bulk as a function of the temperature. In (6), A_0, B, and C are material constants, T denotes the temperature and T_* is a characteristic material-dependent supercooling temperature. One can readily check that all stationary points of f_c are necessarily uniaxial and that there are three characteristic temperatures: (i) $T = T_*$ below which the isotropic phase is unstable, (ii) $T_{IN} = T_* + \frac{B^2}{27A_0C}$ associated with a first-order isotropic-nematic phase transition and (iii) the nematic superheating temperature, $T_{**} = T_* + \frac{B^2}{24A_0C}$, above which ordered nematic states do not exist. For temperatures $T < T_{IN}$, the condensation enforces a uniaxial scalar order parameter, $S = S_{eq}(T) = \frac{B+\sqrt{B^2-24AC}}{4C}$, in the bulk and for temperatures, $T > T_{IN}$, f_c pushes the system towards the disordered isotropic phase. The elastic energy density penalizes any spatial inhomogeneities in the system and we work within the simplest one-constant approximation in (7). The elastic constant is denoted by $L > 0$ in (7). The surface anchoring energy density, $f_s^{(i)}$, enforces a preferred orientation, encoded by $\mathbf{Q}_s^{(i)}$, on the i-th lateral surface. The anchoring coefficient, $w^{(i)}$, is a measure of the strength of the surface anchoring and the $w^i \to \infty$ limit is the strong anchoring limit (also see [21] for comparisons between strong and weak anchoring). Whilst the elastic energy coerces the system towards a spatially homogeneous or uniform state, the condensation energy promotes uniform uniaxial bulk order given by $S = S_{eq}(T)$. However, both conditions cannot typically be satisfied in confined geometries because of boundary conditions, resulting in inhomogeneous pattern formation. In what follows, we compare the competing effects of the elastic contributions, condensation term and the surface effects by means of two different length scales: a material-dependent length scale known as the bare biaxial correlation length and the surface extrapolation length, which capture the relative effects of the elastic and surface contributions respectively [13, 18].

3 Modelling framework

3.1 Geometry

We study nematic samples inside a 3D well with square cross-section, $\mathcal{B} \subset \mathbb{R}^3$, given by

$$\mathcal{B} = \left\{(x, y, z) \in \mathbb{R}^3; 0 \leq x, y \leq R, 0 \leq z \leq h\right\}. \tag{9}$$

In (9), h is the well height, R is the lateral dimension and $h \ll R$, consistent with the assumptions in [20, 21]. We take $h = \frac{R}{10}$. The coordinate unit-vectors are denoted by $(\overrightarrow{e}_x, \overrightarrow{e}_y, \overrightarrow{e}_z)$. The boundary plates are located at $\{x = 0,\ R\}$, $\{y = 0,\ R\}$, $\{z = 0,\ h\}$ and all plates are treated to induce tangent or planar degenerate boundary conditions. Further, we assume that the structural characteristics only depend on the spatial coordinates (x, y) and are independent of the vertical z-coordinate; an assumption often used for shallow wells [20, 21]. The tangent boundary conditions are implemented using a combination of natural boundary conditions, strong and weak anchoring. We impose natural boundary conditions on the top and bottom faces, $z = 0$ and $z = h$. All numerical simulations are initialized using planar initial conditions. The planar initial conditions, combined with the natural boundary conditions, suffice to ensure that the solutions respect the planar degenerate conditions on the top and bottom plates i.e. no particular direction in the (x, y)-plane is distinguished or singled out. We enforce the tangent boundary conditions on the lateral surfaces, $x = \{0, R\}$ and $y = \{0, R\}$, via Dirichlet conditions/strong anchoring or weak anchoring/surface energies. In the strong anchoring case, the corresponding $\mathbf{Q}$-tensor is prescribed to be strictly uniaxial on the lateral surfaces, with director parallel to $\overrightarrow{e}_x$ and $\overrightarrow{e}_y$, on the xz and yz-surfaces respectively.

3.2 Parametrization

We adopt the following 3D parametrization of the $\mathbf{Q}$-tensor order parameter, as given in [13, 17]

$$\mathbf{Q} = (q_3+q_1)\,\overrightarrow{e}_x\otimes\overrightarrow{e}_x+(q_3-q_1)\,\overrightarrow{e}_y\otimes\overrightarrow{e}_y+q_2(\overrightarrow{e}_x\otimes\overrightarrow{e}_y+\overrightarrow{e}_y\otimes\overrightarrow{e}_x)-2q_3\,\overrightarrow{e}_z\otimes\overrightarrow{e}_z, \tag{10}$$

where q_1, q_2, and q_3 are independent of z and only depend on x and y. We assume $\overrightarrow{e}_3 = \overrightarrow{e}_z$ is always an eigenvector of $\mathbf{Q}$. The remaining two eigenvectors are allowed to rotate with respect to the reference frame, $(\overrightarrow{e}_x, \overrightarrow{e}_y)$, by an angle $\varphi \in [0, \pi)$. We have

$$\begin{aligned}
\overrightarrow{e}_1 &= \cos\varphi\,\overrightarrow{e}_x + \sin\varphi\,\overrightarrow{e}_y, \\
\overrightarrow{e}_2 &= -\sin\varphi\,\overrightarrow{e}_x + \cos\varphi\,\overrightarrow{e}_y, && (11)\\
\overrightarrow{e}_3 &= \overrightarrow{e}_z. && (12)
\end{aligned}$$

The parameter q_2 is a measure of the departure of the eigenframe, $(\overrightarrow{e}_1, \overrightarrow{e}_2, \overrightarrow{e}_3)$, from the Cartesian frame, $(\overrightarrow{e}_x, \overrightarrow{e}_y, \overrightarrow{e}_z)$ and the two frames coincide when $q_2 = 0$. The eigenvalues $\{s_i\}$ are explicitly given by $s_1 = q_3 + \sqrt{q_1^2 + q_2^2}$, $s_2 = q_3 - \sqrt{q_1^2 + q_2^2}$ and $s_3 = -2q_3$. In particular, the biaxiality parameter is defined to be

$$\beta^2(q_1, q_2, q_3) = 1 - 6\frac{\left(6\sqrt{(q_1^2 + q_2^2)}q_3 - 6q_3^3\right)^2}{\left(6q_3^2 + 2\left(q_1^2 + q_2^2\right)\right)^3}. \tag{13}$$

The condition, $\sqrt{q_1^2 + q_2^2} = 0$, corresponds to the exchange of eigenvalues, $s_1 \leftrightarrow s_2$, in the nematic phase [9].

We briefly compare the parametrization (10) with the parametrization in [21] where the authors study strictly two-dimensional LC configurations on a square domain; the $\mathbf{Q}$-tensor is then given by

$$\mathbf{Q} = S\left(\overrightarrow{e}_1 \otimes \overrightarrow{e}_1 - \overrightarrow{e}_2 \otimes \overrightarrow{e}_2\right). \tag{14}$$

Here, $\mathrm{tr}\mathbf{Q}^3 = 0$, the biaxiality parameter in (13) has no physical meaning and all defects correspond to isotropic regions or locally melted regions [21]. The 2D parametrization (14) can be related to (10) by

$$\mathbf{Q} = S\left(\overrightarrow{e}_1 \otimes \overrightarrow{e}_1 - \overrightarrow{e}_2 \otimes \overrightarrow{e}_2\right) + q_3\left(\overrightarrow{e}_z \otimes \overrightarrow{e}_z - \frac{\mathbf{I}}{3}\right). \tag{15}$$

The representation (10) contains more information than (14) since it allows us to investigate structural variations in both q_3 and β^2, both of which are outside the scope of the 2D representation (14). In particular, the parametrization (10) can resolve the rich biaxial structure of defect cores.

On the faces, $x = 0$ and $x = R$, we set the preferred $\mathbf{Q}$-tensor to be

$$\mathbf{Q}_s^{(x)} \equiv \mathbf{Q}(0, y, z) = \mathbf{Q}(R, y, z) = \frac{S_{eq}}{3}\left(-\overrightarrow{e}_x \otimes \overrightarrow{e}_x + 2\overrightarrow{e}_y \otimes \overrightarrow{e}_y - \overrightarrow{e}_z \otimes \overrightarrow{e}_z\right) \tag{16}$$

where $S_{eq} = \frac{B + \sqrt{B^2 - 24AC}}{4C}$. On the boundaries $y = 0$ (bottom) and $y = R$ (top), we set

$$\mathbf{Q}_s^{(y)} \equiv \mathbf{Q}(x, 0, z) = \mathbf{Q}(x, R, z) = \frac{S_{eq}}{3}\left(2\overrightarrow{e}_x \otimes \overrightarrow{e}_x - \overrightarrow{e}_y \otimes \overrightarrow{e}_y - \overrightarrow{e}_z \otimes \overrightarrow{e}_z\right). \tag{17}$$

For systems with Dirichlet conditions, we set $\mathbf{Q} = \mathbf{Q}_s^{(x)}$ and $\mathbf{Q} = \mathbf{Q}_s^{(y)}$ on the respective lateral surfaces. For systems with finite anchoring, we use the prescribed $\mathbf{Q}$-tensors in (16) and (17) as the preferred state, $\mathbf{Q}_s^{(i)}$, in the surface anchoring energy density in (8). On the surfaces $z = 0$ and $z = h$, we impose natural boundary conditions i.e. require that

$$\frac{\partial \mathbf{Q}}{\partial \nu} = 0 \quad \text{on } z = 0, h, \tag{18}$$

where $\nu = \pm\overrightarrow{e}_z$ is the outward normal to these faces in the (x, y)-plane. This is consistent with the assumed invariance in the z-direction and when combined with planar initial conditions for numerical simulations, ensures that the leading eigenvector (with the largest positive eigenvalue) of the $\mathbf{Q}$-solutions respects the tangent boundary conditions.

3.3 Scaling

Let t be a dimensionless temperature defined to be $t = (T - T_*)/(T_{**} - T_*)$. Therefore, $t(T = T_*) = 0$, $t(T = T_{IN}) = 8/9$ and $t(T = T_{**}) = 1$. We define

$$\tau = 1 + \sqrt{1 - t}. \tag{19}$$

The equilibrium uniaxial order parameter can then be expressed as

$$S_{eq} = S_{**}\tau \tag{20}$$

where $S_{**} = S_{eq}(T_{**}) = \frac{B}{4C}$.

The structural characteristics of static LC equilibria are dictated by a complex interplay between material properties and surface anchoring effects. The key material length-scale is the biaxial correlation length defined to be

$$\xi_b = \frac{\xi_b^{(0)}}{\sqrt{\tau}}, \tag{21}$$

where $\xi_b^{(0)} = 2\sqrt{LC}/B$ is the bare biaxial correlation length [1, 14, 23]. For conventional nematics, $\xi_b^{(0)} \sim 2 - 5$ nm [1]. The strength of the surface interactions is traditionally described in terms of the surface extrapolation length [14, 23].

$$d_e^{(i)} = \frac{L}{w^{(i)}}. \tag{22}$$

Typical values of L are around $10^{-12}N$ and $w^i \in \left(10^{-8}, 10^{-3}\right)\ N/m$ [8].

We further define the following dimensionless quantities: $\widetilde{\mathbf{Q}} = \mathbf{Q}/S_{**}$, $\widetilde{x} = x/R$, $\widetilde{y} = y/R$, $\widetilde{z} = z/R$, $\widetilde{\nabla} = R\nabla$, $\widetilde{F} = F/F_0$, where $F_0 = LS_{**}^2R^3/(2\xi_b^{(0)2})$. In what follows, we drop the tildes from the dimensionless variables and all subsequent text is to be interpreted in terms of the dimensionless variables. The dimensionless free energy F is given as in (5), and the corresponding

dimensionless free energy densities are defined to be

$$
\begin{aligned}
f_c &= \frac{\tau}{6} Tr\mathbf{Q}^2 - \frac{2}{3} Tr\mathbf{Q}^3 + \frac{1}{8}\left(Tr\mathbf{Q}^2\right)^2 = \\
&\quad \frac{\tau}{3}\left(q_1^2 + q_2^2 + 3q_3^2\right) - 4q_3\left(q_1^2 + q_2^2 - q_3^2\right) + \frac{1}{2}\left(q_1^2 + q_2^2 + 3q_3^2\right)^2, \\
f_e &= \left(\frac{\xi_b^{(0)}}{R}\right)^2 |\nabla\mathbf{Q}|^2 = 2\left(\frac{\xi_b^{(0)}}{R}\right)^2 \left(3\left|\nabla q_3\right|^2 + \left|\nabla q_1\right|^2 + \left|\nabla q_2\right|^2\right), \\
f_s^{(i)} &= \frac{\xi_b^{(0)2}}{d_e^{(i)} R} Tr\left(\mathbf{Q} - \mathbf{Q}_s(\varphi_s)\right)^2 = \\
&\quad \frac{2}{3}\left(\frac{\xi_b^{(0)}}{R}\right)\left(\frac{\xi_b^{(0)}}{d_e^{(i)}}\right)\left(9q_3^2 + 3q_1^2 + 3q_2^2 - 3q_3\tau + \tau^2 - 3q_1\tau\cos(2\varphi_s) - 3q_2\tau\sin(2\varphi_s)\right).
\end{aligned}
$$

In the expression for f_s above, the angle φ_s is either $\varphi_s = 0$ (plates at $y = 0$ and $y = R$) or $\varphi_s = \pi/2$ (plates at $x = 0$ and $x = R$). The strong anchoring limit, $w^{(i)} \to \infty$, corresponds to vanishing surface extrapolation length, $d_e^{(i)} \to 0$. We now offer some heuristic insight on pattern formation within the LC wells. On the one hand, if τ is large compared to the scaled elastic constant, $\left(\frac{\xi_b^{(0)}}{R}\right)^2$, then the solution will predominantly minimize the condensation energy i.e. be largely uniaxial with constant order parameter, $S = S_{eq}(T)$ (at least away from defects). On the other hand, if τ and $\left(\frac{\xi_b^{(0)}}{R}\right)^2$ are of comparable magnitude, then there is a relatively small energetic penalty for biaxiality since deviations from the condensation energy minima (uniaxial phases with $S = S_{eq}(T)$) are not energetically expensive. Similarly, if $\frac{\xi_b^{(0)}}{R} \gg \frac{\xi_b^{(0)}}{d_e^{(i)}}$, then the uniaxial boundary conditions are relatively weakly implemented on the lateral surfaces and the system has greater freedom to adopt almost "spatially homogeneous" or uniform states. This, in turn, allows the system to avoid complex uniaxial-biaxial structural transitions or the OR phenomenon for sufficiently weak anchoring. In the next section, we compute phase diagrams for uniaxial-biaxial structural transitions, as a function of R, anchoring strength and temperature, and these phase diagrams corroborate our heuristic insights.

3.4 Euler Lagrange equations

We use standard methods in calculus of variations to compute the Euler-Lagrange equations for extremal points of the LdG energy functional [25]. The Euler-Lagrange equations are a coupled system of elliptic partial differential equations for (q_1, q_2, q_3) as shown below:

$$\left(\frac{\xi_b^{(0)}}{R}\right)^2 \Delta_\perp q_1 - \frac{\tau}{6} q_1 + 2 q_3 q_1 - \frac{q_1}{2}(3q_3^2 + q_1^2 + q_2^2) = 0, \tag{23}$$

$$\left(\frac{\xi_b^{(0)}}{R}\right)^2 \Delta_\perp q_2 - \frac{\tau}{6} q_2 + 2 q_2 q_3 - \frac{q_2}{2}(3q_3^2 + q_1^2 + q_2^2) = 0, \tag{24}$$

$$\left(\frac{\xi_b^{(0)}}{R}\right)^2 \Delta_\perp q_3 - \frac{\tau}{6} q_3 + \frac{1}{3}(q_1^2 + q_2^2 - 3q_3^2) - \frac{q_3}{2}(3q_3^2 + q_1^2 + q_2^2) = 0, \tag{25}$$

where $\Delta_\perp = \frac{\partial^2}{\partial x^2} + \frac{\partial^2}{\partial y^2}$.
The boundary conditions on the plates $x = 0$ and $x = R$ are

$$\frac{\partial q_1}{\partial x} = \mp \frac{R}{d_e^{(x)}} \left(q_1 - \frac{\tau}{2}\right), \tag{26}$$

$$\frac{\partial q_2}{\partial x} = \mp \frac{R}{d_e^{(x)}} q_2, \tag{27}$$

$$\frac{\partial q_3}{\partial x} = \mp \frac{R}{d_e^{(x)}} \left(q_3 - \frac{\tau}{6}\right), \tag{28}$$

$-(+)$ in $\mp$ refers to the right (left) plate and $d_e^{(x)}$ is a measure of the anchoring strength, $w_s^{(x)}$ on each plate.

Similarly, we have the following boundary conditions on the plates $y = 0$ and $y = R$

$$\frac{\partial q_1}{\partial y} = \mp \frac{R}{d_e^{(y)}} \left(q_1 + \frac{\tau}{2}\right), \tag{29}$$

$$\frac{\partial q_2}{\partial y} = \mp \frac{R}{d_e^{(y)}} q_2, \tag{30}$$

$$\frac{\partial q_3}{\partial y} = \mp \frac{R}{d_e^{(y)}} \left(q_3 - \frac{\tau}{6}\right), \tag{31}$$

where $-(+)$ in $\mp$ refers to the top (bottom) plate and $d_e^{(y)}$ is a measure of the relative anchoring strength. The corresponding strong anchoring conditions are $\left\{q_1 = -\frac{\tau}{2}, q_2 = 0, q_3 = \frac{\tau}{6}\right\}$ on $y = \{0, R\}$ and $\left\{q_1 = \frac{\tau}{2}, q_2 = 0, q_3 = \frac{\tau}{6}\right\}$ on $x = \{0, R\}$. The strong anchoring or Dirichlet conditions can be recovered from (26)-(28) and (29)-(31) in the limit, $d_e^{(x)} \to 0$ and $d_e^{(y)} \to 0$ respectively.

We solve the Euler-Lagrange equations (23 - 25) and the boundary constraints (26 - 31) using relaxation methods that have been successful in the study of static LC textures with topological defects [25, 13]. These methods compute the static solutions, (q_1, q_2, q_3), by mimicking a dynamic gradient-flow like procedure along which the total free energy continuously decreases

till the equilibrium is attained, for an explicitly prescribed initial condition. We use three different kinds of initial conditions: (i) bulk uniaxial alignment along $\overrightarrow{e}_x$, (ii) bulk uniaxial alignment along $\overrightarrow{e}_x + \overrightarrow{e}_y$, or (iii) the isotropic phase with $\mathbf{Q} = 0$. The $\mathbf{Q}$-tensor is recovered from the solution, (q_1, q_2, q_3), by using the parameterization (10). The solutions are robust with respect to different choices of initial conditions and we thus, deduce that they are numerically stable.

4 Results

Macroscopic wells with $R \gg \xi_b^0$, e.g. micron-sized wells, have already been modelled in detail in [20, 21]. We focus on nano-scale wells, with R comparable to ξ_b^0, in this paper. We use fixed values of L, B, C and hence, the bare biaxial correlation length, $\xi_b^{(0)} = \sqrt{\frac{4LC}{B^2}}$ is a constant throughout this paper. We are interested in structural changes induced by decreasing the ratio $\eta = R/\xi_b^{(0)}$. In simulations, we work with temperatures below T_*, corresponding to $\tau > 2$ (see Eq.(19)). Previous work indicates that biaxial textures are more likely in this low-temperature regime, compared to the high-temperature regime with temperatures above the nematic-isotropic transition temperature. [17, 16]. For example, we carry out illustrative simulations with $\tau = 4$. The same temperature was chosen in the reference [17], where the authors study OR patterns in "classical" hybrid planar cells.

4.1 Diagonal Structure with Defects (DSD)

In Figures 1, 2a and 3, we consider the specific example of a LC well with $R = 4.5\xi_b^0$ (of the order of 10 to 20 nm), at temperature $\tau = 4$ (with $t = -8$ in (19)), with strong anchoring conditions on the lateral surfaces. The Dirichlet conditions (see (16) and (17)) induce an alignment mismatch along the four vertical edges and we consequently, obtain four line defects along the four vertical edges in the z-direction. In Figure 1 and Figure 2a, we plot the spatial profile of β^2 and in Figure 3, we plot the leading eigenvector (with the largest positive eigenvalue) of the computed $\mathbf{Q}$-tensor. This eigenvector profile is strongly reminiscent of the diagonal solution reported in [20, 21] and evidently has a diagonal profile across the square (x,y) cross-section. For a purely uniaxial solution with two degenerate eigenvalues, this eigenvector would simply be the director in (2). From Figure 3, it is clear that the leading eigenvector has four point defects at the four square vertices and each point defect can be regarded as a quarter of $+1$ or -1-degree point defect i.e. the defects at the top left and bottom right are a quarter of $+1$-degree radial defects and the defects at the bottom left and top right are a quarter of -1-degree point defects. In other words, the leading eigenvector rotates by 90 degrees between a pair of coincident square edges.

In Figures 1 and 2a, we study the structural characteristics near each defect core in terms of β^2; the profile is somewhat similar to the classical OR phenomenon studied in [9] etc. We have two intersecting faces at each vertical edge and these faces enforce strictly uniaxial alignments with mutually perpendicular directors, along $\overrightarrow{e}_x$ and $\overrightarrow{e}_y$ respectively, and positive scalar order parameter. As is evident from the plots, the LC state mediates between these two uniaxial "boundary" states by means of an intermediate biaxial pear-shaped lobe. This biaxial lobe has a rim of maximal biaxiality ($\beta^2 = 1$) and the interior of the lobe has suppressed biaxiality.

In Figure 4, we look at β^2 along a square diagonal. We see that β^2 monotonically increases from the vertex to the rim of the biaxial lobe, where $\beta^2 \approx 1$. Here, β^2 has a local maximum and this local maximum is followed by a local minimum near the center of the diagonal. At the center, we are relatively far away from square vertices. Then β^2 attains a local maximum at the rim of the biaxial lobe encasing the diagonally opposite vertex and finally decreases to zero as we hit the opposite vertex. The β^2-profile is characterized by two maxima, one for each square vertex, separated by a local minimum. The biaxial defect lobes are asymmetric in shape, in response to the neighbouring defect cores at the different vertical edges. One could define the characteristic linear defect core size to be the distance from the vertex to the nearest rim of maximal biaxiality, measured along the square diagonal. This length is roughly given by ξ_b, as is expected from previously reported results in the literature [14, 13, 23, 17]. We refer to this diagonal profile, with biaxial defect cores near the vertical edges, as the Diagonal Structure with Defects (DSD) in the subsequent text.

4.2 Well Order-Reconstruction Structure (WORS)

We study structural transitions induced by gradually decreasing the ratio $\eta = R/\xi_b^{(0)}$. In Figures 2a - 2d, we demonstrate a sequence of $\beta^2(x, y)$ textures obtained by gradually decreasing the ratio, $\eta = R/\xi_b^{(0)}$, at fixed temperature $\tau = 4$, with strong anchoring conditions. As η decreases, the biaxial defect lobes become larger (relative to domain size), overlap and eventually connect to yield a 2D star-shaped rim of maximal biaxiality connecting the four vertices. We have numerically verified that the star-shaped biaxial ring separates uniaxial states with negative order parameter inside the ring from uniaxial states with positive order parameter outside the ring. [1] In this sense, this is a fully 2D OR pattern connecting the four vertices.

If we follow β^2 along a small circular arc, centered around a square vertex, we expect to see the following sequence of characteristic states: (i) positive uniaxiality (positive scalar order parameter) with $\beta^2 = 0$, (ii) max-

[1] We interpret regions with $\beta^2 < 0.01$ as being uniaxial for practical purposes. We note that β^2 may not, strictly speaking, vanish at any point inside the well.

imal biaxiality with $\beta^2 = 1$, (iii) negative uniaxiality (negative scalar order parameter)with $\beta^2 = 0$, (iv) maximal biaxiality with $\beta^2 = 1$, (v) positive uniaxiality with $\beta^2 = 0$. By symmetry, we expect to see state (iii) along the square diagonal. In Figure 4, we monitor the structural characteristics along a square diagonal at the fixed temperature $\tau = 4$. In Figure 4*a*, we plot $\beta^2(\eta)$, measured along the square diagonal, for different values of η. For relatively large η, say $\eta = 4.5$, the β^2-profile has two distinct maxima. This corresponds to the DSD structure reported above. We refer to the two maxima (where $\beta^2 = 1$) in the regions $x < 0.5$ and $x > 0.5$ as the *left peak* and *right peak*respectively. As η decreases, the maxima approach each other and coalesce at $\eta = 3.39$. For smaller values of η, say $\eta = 3.3$, the β^2-maximum is suppressed in magnitude i.e. is smaller than unity. At $\eta = \eta_c = 3.28 \pm 0.01$, β^2 vanishes along the square diagonal.

In Figure 4*b*, we compute $< \beta^2 >_d$ and β^2_m as a function of η, representing average value and maximal value of β^2 along the well diagonals, respectively. Additionally, we plot the position of the left peak, denoted by x_m in the region $x \in [0, R/2]$. Further, we also plot the spatial average of β^2 across the square cross-section, denoted by $< \beta^2(x, y) >$, as a function of η. From Figure 4*b*, we have that the global OR profile is established at $\eta = \eta_c = 3.28 \pm 0.01$, for which $\beta^2_m =< \beta^2 >_d = 0$. The quantities, $\beta^2_m =< \beta^2 >_d = 0$, for all $\eta \leq \eta_c$. For $\eta \leq \eta_c$, we have a purely uniaxial LC state, with negative scalar order parameter, along the square diagonal. The corresponding critical radius, $R_c = \eta_c \xi_b^{(0)}$. The average degree of biaxiality, $< \beta^2 > (\eta) \approx 0.4$ for $\eta \leq \eta_c$. Since $< \beta^2 >_d = 0$ for $\eta \leq \eta_c$, x_m is not defined for $\eta < \eta_c$. In what follows, we refer to the star-shaped biaxial OR pattern in Figure 2*d* as the **Well Order Reconstruction Pattern (WORS)**. We define the onset of the WORS by two quantitative measures: $\beta^2_m =< \beta^2 >_d = 0$ along the square diagonal. Our simulations suggest that the DSD-WORS transition is continuously achieved by decreasing η and hence, this is a **second-order transition**.

4.3 Phase diagrams

In Figures 6*a*, we numerically study the dependence of the critical radius, $R_c/\xi_b^{(0)}$, on the scaled temperature $t = (T - T_*)/(T_{**} - T_*)$, with strong anchoring conditions. As above, R_c is signalled by vanishing β^2 along the square diagonal. As t increases towards $T = T^*$ (the temperature at which the isotropic phase loses stability), R_c increases steeply. This steep ascent can be explained on the grounds that the condensation energy penalty for deviations from the uniaxial state with $S = S_{eq}(T)$, decreases as t increases. Hence, biaxial order reconstruction patterns (such as the WORS pattern) become increasingly energetically viable, and hence, observable as t increases.

In Figure 6*b*, we plot $R_c/\xi_b^{(0)}$ versus the anchoring strength, $\frac{\xi_b^{(0)}}{d_e^{(0)}}$. We impose equal anchoring strength on all four lateral surfaces and work with two different temperatures, $t = -8$ and $t = 0$ respectively. These temperatures correspond to qualitatively different temperature regimes (i.e. $T << T_*$ and $T = T_* < T_{IN}$). We observe a slowly increasing profile of R_c versus $\frac{1}{d_e^{(0)}}$ for both temperatures. From the reasoning in Figure 6*a*, the critical threshold R_c is always higher for higher temperatures. Further, R_c rapidly saturates to a limiting value as $\frac{1}{d_e^{(0)}}$ increases; this limiting value is simply the strong anchoring limit. For $t = -8$ or equivalently for $\tau = 4$, this limiting value is $R_c = 3.28\xi_b^{(0)}$ which coincides with the critical value yielded by the strong anchoring experiments in Figure 4. As $\frac{1}{d_e^{(0)}}$ decreases or equivalently as the anchoring strength decreases, the uniaxial boundary conditions are relatively weakly implemented. This effectively increases the lateral well size since the system has anchoring freedom on the lateral surfaces and hence, does not need to strictly match or satisfy the competing preferred uniaxial states on intersecting edges. The WORS profile ceases to exist for anchoring strengths below than a certain critical threshold. For such cases, the anchoring conditions are not strong enough to support geometrically imposed frustration.

4.4 Comparison with classical OR structure

In Figures 5*a*-5*c*, we compare the WORS pattern with the classical OR pattern reported in a batch of numerical papers [10, 17, 23]. In Figure 5*a*, we plot $\beta^2(x, y)$ across the square cross-section and observe a distinct star-shaped rim of maximal biaxiality, $\beta^2(x, y) = 1$, that separates regions with positive uniaxial and negative uniaxial ordering outside and inside the rim, respectively. In Figure 5*b*, we plot $-\beta^2(x, y)$ to emphasize the cross-shaped uniaxial ordering (i.e. $\beta^2 = 0$) along diagonals. Here, the local eigenframe of $\mathbf{Q}$ coincides with the $\{\overrightarrow{e}_x, \overrightarrow{e}_y, \overrightarrow{e}_z\}$-laboratory frame and $q_2 = 0$ throughout the square domain in (10).

We can reproduce the classical OR phenomenon in our framework by enforcing conflicting planar and homeotropic anchoring on the plates at $y = 0$ and $y = R_y$ respectively, whilst imposing natural boundary conditions on $x = 0$ and $x = R_x$. Equivalently, we require that

$$\mathbf{Q}(x, 0, z) = \frac{S_{eq}}{3}\left(2\overrightarrow{e}_x \otimes \overrightarrow{e}_x - \overrightarrow{e}_y \otimes \overrightarrow{e}_y - \overrightarrow{e}_z \otimes \overrightarrow{e}_z\right) \tag{32}$$

and

$$\mathbf{Q}(x, R_y, z) = \frac{S_{eq}}{3}\left(2\overrightarrow{e}_y \otimes \overrightarrow{e}_y - \overrightarrow{e}_x \otimes \overrightarrow{e}_x - \overrightarrow{e}_z \otimes \overrightarrow{e}_z\right). \tag{33}$$

We then progressively decrease the distance, R_y, whilst keeping R_x fixed, at constant temperature $\tau = 4$. At a critical value, $\eta_c^{(CL)} = 2.45$ (the superscript $^{(CL)}$ marks the *classical* order reconstruction transition), we observe

a structural transition into the classical OR pattern and the classical OR pattern is observed for all $\eta < \eta^{(CL)}$. We plot β^2 for the classical OR case in Figure 5c and clearly see two sheets of maximal biaxiality ($\beta^2 = 1$) enclosing a sheet of negative uniaxiality ($\beta^2 = 0$). On comparing Figures 5a and 5c, it is clear that the WORS is qualitatively different to the classical OR pattern; the WORS arises from mutually perpendicular uniaxial alignments on four pairs of coincident faces whereas the classical OR phenomenon arises from mutually perpendicular uniaxial alignments on pairs of parallel edges. Whilst the WORS is observed for $\eta < 3.28$, the classical OR pattern is observed for $\eta < 2.45$ i.e. the WORS pattern has a broader window of stability compared to the classical OR case. We do not have rigorous explanations for these effects but elevated stability thresholds can be potentially attributed to the topological defects present in the WORS. Similar effects have been observed in hybrid cylindrical cells with a boojums on bounding plates [23].

4.5 Interior Defects and the WORS pattern

We demonstrate a DSD-WORS structural transition induced by locally melted regions within the DSD structure. This could, in practice, be realized either by focussing a narrow laser beam within a well or by introducing a nanoparticle (NP) imposing melting at the NP-LC interface. We numerically enforce a melted square cavity of lateral size r_m, at the center of the well. Therefore, we enforce $\mathbf{Q}(\frac{R}{2} \pm r_m/2, \frac{R}{2} \pm r_m/2, z) = 0$. We take $\tau = 4$, $\frac{R}{\xi_b} = 4.5$, with strong anchoring conditions as in (16) and (17) and no external fields. In dimensional terms, this describes a well with lateral dimensions between $10 - 20$ nm at a low temperature, well below the transition temperature $T = T_{NI}$. In particular, the DSD is stable in this regime, without the melted region. In Figures 7a, 7b and 7c, we numerically compute LC equilibria in the absence and presence of locally melted regions respectively. We recover the familiar DSD in Figure 7a which exhibits localized biaxial pear-shaped lobes near the square vertices and the vertical well edges. However, in Fig. 7b, we observe a star-shaped rim of maximal biaxiality, characteristic of the WORS. In Figure 7c, we displace the melted region from the centre towards the lower plate at $y = 0$ and lose the WORS. This suggests that the WORS can be efficiently stabilized if the locally melted region is compatible with the structural symmetry of the WORS.

In Figure 8 we study the effect of r_m: the size of the melted region on the DSD-WORS structural transition. We follow $< \beta^2 >$ as a function of η, for different values of r_m. All curve have a slowly decreasing profile till they hit the critical value of $\eta = \eta_c^{(m)}$ and the WORS is stable for all $\eta \leq \eta_c^{(m)}$. It is evident that interior melted regions substantially increase the value of $\eta_c^{(m)}$. For example, we obtain $\eta_c = 3.28 \pm 0.01$ with $r_m = 0$ and calculate $\eta_c^{(m)} = 4.67 \pm 0.01$ for $r_m/R = 0.1$. Hence, the threshold value is increased by roughly 42%.

5 Conclusions

We model and numerically analyze LC textures inside shallow square wells, within the LdG theory for nematic LCs. These wells were first reported in [20] and modelled in the papers [20, 21]. In [20, 21], the authors study large micron-sized wells and perform a strictly two-dimensional study on a square or a rectangle. Our aim is to quantify the effects of nanoconfinement, temperature, boundary conditions on the experimentally observed well textures, with special emphasis on novel biaxial textures. Our work purely focuses on static LC textures and we do not study field-induced or dynamic effects.

We study shallow square wells with cross-sectional dimension R, where R is measured in units of the bare biaxial correlation length, $\xi_b^{(0)}$. We assume that all variables only depend on the spatial coordinates, (x, y), and that they are independent of the z-coordinate. The boundary conditions on the lateral surfaces, $x = \{0, R\}$ and $y = \{0, R\}$, are imposed either via Dirichlet conditions (as in (16) and (17)) or via a surface anchoring energy as in (8). The Dirichlet conditions in (16) and (17) create line defects along the vertical edges. For wells with $R \gg \xi_b$, the static structures are effectively uniaxial away from the edges and are well described by the *diagonal* and *rotated* solutions in [20, 21]. We study wells with $R = O(\xi_b)$ in this paper and obtain two distinct LC states: the DSD and WORS patterns. The DSD pattern is qualitatively similar to the diagonal solution reported in [20, 21] and is only obtained for relatively large wells with $R > R_c$, where the critical length R_c has been computed numerically. The DSD is largely uniaxial away from the vertical line defects and the principal eigenvector has a diagonal profile along the square diagonal on the bottom surface, $z = 0$. There are localized pear-shaped biaxial regions/neighbourhoods near each vertical edge, the rims of which exhibit maximal biaxiality. We believe that the macroscopic properties of the DSD solution are qualitatively similar to the diagonal solution in [20, 21] and our contribution is the resolution of the biaxial defect cores, since biaxiality was not reported in previous work.

We progressively decrease the ratio $\eta = \frac{R}{\xi_b^{(0)}}$ and at a critical value $\eta = \eta_c(\tau)$, (e.g. $\eta_c(4) = 3.28 \pm 0.01$) we observe a global WORS pattern with a star-shaped biaxial ring connecting all four vertical edges. The biaxial ring separates uniaxial states with negative order parameter inside the ring from uniaxial states with positive order parameter outside the ring respectively. The critical value depends on the temperature and anchoring strength on the lateral surfaces. We define quantitative criteria for the onset of the WORS pattern, in terms of the maximum value of β^2 (β_m^2) and the average value of β^2 ($< \beta^2 >_d$) along a square diagonal. The onset is defined by the critical value of η for which $\beta_m^2 =< \beta^2 >_d = 0$, denoted by eta_c, and the WORS is the only observed state for $\eta \leq \eta_c$. The DSD-WORS transition is a continuous transition and we interpret stable states with $\beta_m^2 =< \beta^2 >_d \neq 0$ for $\eta > \eta_c$

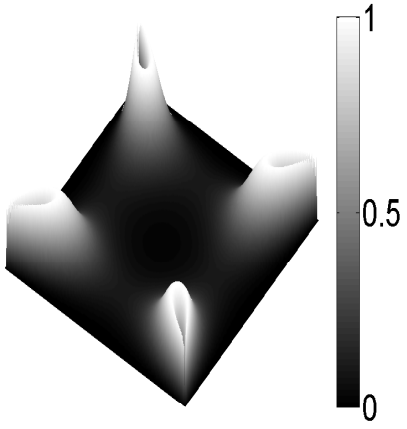

Figure 1: The degree of biaxiality, $\beta^2(x, y)$, in a square well with $R/\xi_b^{(0)} = 4.5$, $\tau = 4$ and strong anchoring conditions. The colour code for $\beta^2 \in [0, 1]$ is on the right side.

as being a variant of the DSD state. Further, we study the dependence of η_c on the temperature and the anchoring strength on the lateral surface, with no external fields in Figure 6. Numerical simulations show that interior locally melted regions, do not substantially alter the symmetry of WORS but substantially increase the stability window of the WORS.

The WORS is a global 2D biaxial texture predicted for nano-confined systems with moderate to strong anchoring conditions, for temperatures below the supercooling temperature. The WORS is qualitatively different to the reported diagonal and rotated solutions in [20, 21]. As such, we expect that it will offer different optical properties, new responses to electric fields etc. Our numerical work can give engineers quantitative information about the scale and shape of nano-scale devices that can support the WORS pattern. Once such devices are actually engineered, one could experimentally measure the electro-optical responses of the WORS pattern, possibly by analogy with similar experimental work on OR patterns in one-dimensional hybrid cells in [18, 24]. Whilst our work sets up a sound foundation for the study of the WORS pattern, there are several directions for further study which include (i) field-induced effects, (ii) study of time-dependent or dynamic phenomena, (iii) effects of elastic anisotropy, (iv) non-cuboid geometries and (v) inclusion of interior defects. Whilst biaxial patterns have been extensively found in the literature; see [14, 13, 23, 19, 10, 9] etc., these reported textures are heavily localized near defects or boundaries. Our work, along with the generalizations cited above, can collectively yield vital information about systems with intrinsic biaxiality and how biaxiality can be exploited for future generations of nano-scale applications.

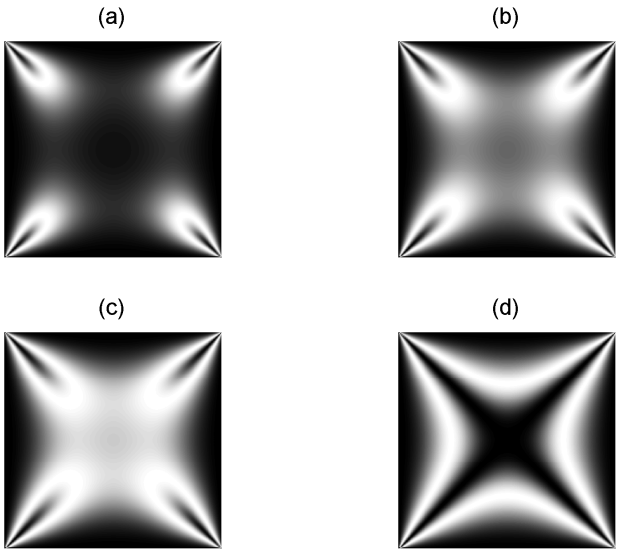

Figure 2: Plots of $\beta^2(x,y)$ with decreasing $\eta = R/\xi_b^{(0)}$, at a fixed temperature $\tau = 4$ and strong anchoring conditions. (a) $\eta = 4.5$, (b) $\eta = 3.8$, (c) $\eta = 3.6$, (d) $\eta = 3$. We observe the WORS below the critical value $\eta_c = 3.28 \mp 0.01$.

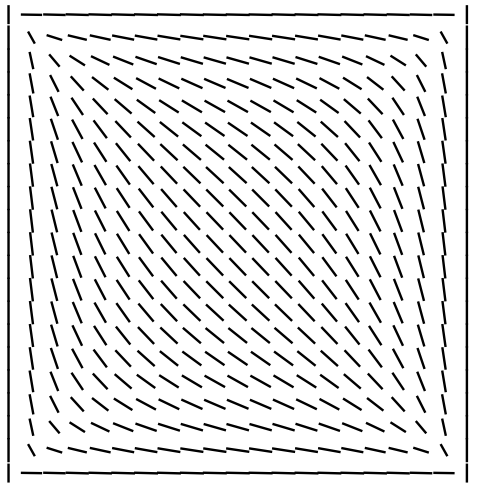

Figure 3: The maximal eigenvector of the **Q**-solution with $R/\xi_b^{(0)} = 4.5$, $\tau = 4$ and strong anchoring conditions.In the uniaxial limit, this eigenvector is simply the nematic director field. The corresponding $\beta^2(x,y)$ dependence is plotted in Fig. 1.

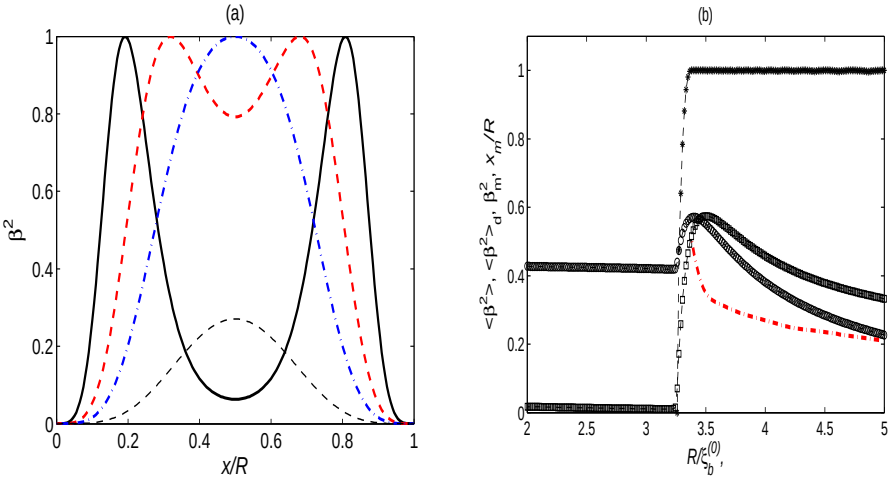

Figure 4: Onset of WORS structure with $\tau = 4$ and strong anchoring conditions. (a) Plots of $\beta^2(x)$ along the well diagonal, where x/R is the scaled distance along the square diagonal measured from the bottom left vertex. $\eta = 4.5$, thick black full line; $\eta = 3.5$, thick red dashed line; $\eta = 3.39$, thick blue dash-dash line; $\eta = 3.3$, thin black dashed line. (b) Structural characteristics of WORS: $< \beta^2 >_d$ (open squares), $< \beta^2 >$ (open spheres), β_m^2 (asterisks)and x_m (red dashed line)as a function of η. $\beta_m^2 =< \beta^2 >_d = 0$ for the WORS and x_m is not defined for $\eta < \eta_c$.

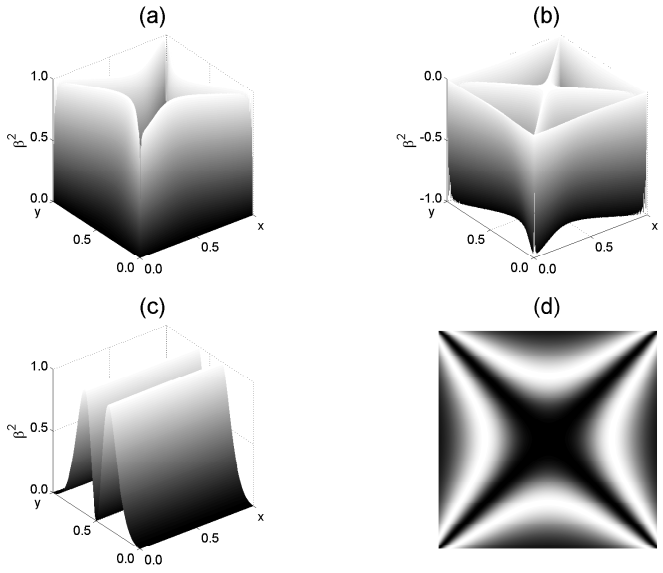

Figure 5: $\beta^2(x, y)$ plots for OR patterns with $\tau = 4$. (a) and (b): the WORS texture in a square well; $\eta = 3$, strong anchoring condition. (c) the *classical* OR structure within a hybrid cell; $\eta = 2.5$, strong anchoring condition. (d) WORS (top view), $\eta = 3$ with weak anchoring condition ($R/d_e = 5$).

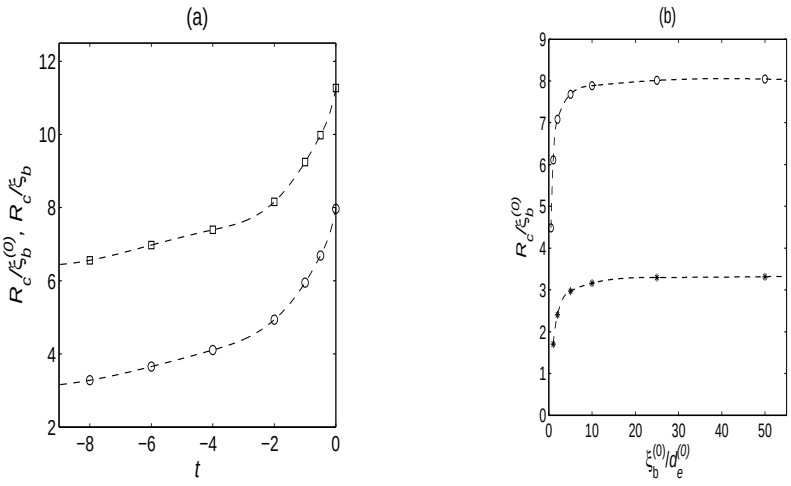

Figure 6: Effect of temperature and anchoring strength on the stability of WORS. Symbols designate points where thresholds are calculated. Lines are guides for the eye. (a) Temperature variation of $\eta_c^* = \sqrt{\tau}\eta_c = R_c/\xi_b$ (squares) and $\eta_c = R_c/\xi_b^{(0)}$ (spheres) with strong anchoring condition. (b) Impact of anchoring strength on η_c for $t = -8$ (asterisk symbols) and $t = 0$ (spheres).

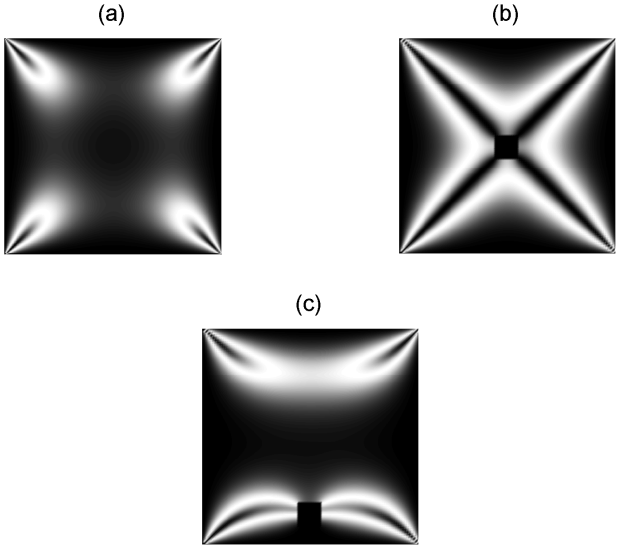

Figure 7: Effect of interior melted region on stability of nematic structures with parameters $R/\xi_b^{(0)} = 4.5$, $\tau = 4$, strong anchoring. (a) The DSD in the absence of a melted region. (b) The WORS with a melted region at the center of the well. (c) The melted region is displaced below the center of the well.

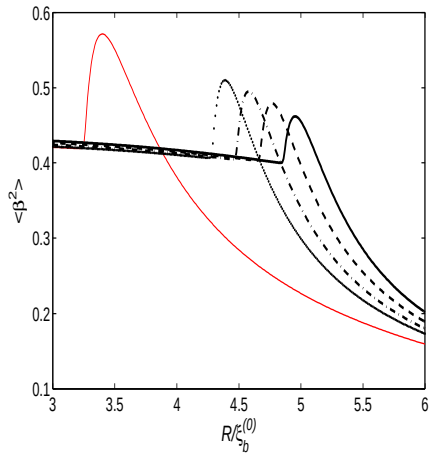

Figure 8: The average degree of biaxiality as a function of $\eta = R/\xi_b^{(0)}$ for structures (i) without (full red thin line) and with melted region (black thick lines) revealing the DSD-WORS structural transition. The plots are computed with $\tau = 4$ and strong anchoring conditions. The linear size r_m of square melted region is equal to (ii) $r_m/R = 0.1$ (thick full line), (iii) $r_m/R = 0.08$ (thick dashed line), (iv) $r_m/R = 0.06$ (thick dash-dash line), (v) $r_m/R = 0.04$ (thick dotted line). The structural transition takes place at (i) $\eta_c = 2.28 \pm 0.01$, (ii) $\eta_c^{(m)} = 4.86 \pm 0.01$, (iii) $\eta_c^{(m)} = 4.67 \pm 0.01$, (iv) $\eta_c^{(m)} = 4.48 \pm 0.01$, (v) $\eta_c^{(m)} = 4.29 \pm 0.01$.

Acknowledgements: AM is supported by an EPSRC Career Acceleration Fellowship EP/J001686/1, an Oxford Centre for Collaborative Applied Mathematics (OCCAM) Visiting Fellowship and a Keble Research Grant, Keble College. AM and SK thank the Isaac Newton Institute, University of Cambridge for a Visiting Fellowship as part of the "Mathematics of Liquid Crystals" programme. SK thanks OCCAM and the University of Bath for supporting collaborative trips in connection to this project.

References

[1] M.Ambrozic, F.Bisi and E.G.Virga, 2008, Continuum Mechanics and Thermodynamics, 20, pp 193-218.

[2] B. Bahadur, Liquid Crystals: Applications and Uses. World Scientific, Singapore, 1990.

[3] M. Kleman and O.D. Lavrentovich, Soft Matter Physics. Springer, Berlin, 2002.

[4] Y.Youngwoo et.al, 2009, Physical Review E, 79, pp 041701.

[5] G.Lombardo et.al, 2008, Physical Review E, 77, pp 051708.

[6] G.Carbone et. al, 2009, Physical Review Letters, 103, pp 167801.

[7] N. Mermin, 1979, Reviews of Modern Physics, 51, pp 591.

[8] N.J.Mottram and C.Newton, Introduction to **Q**-tensor Theory. University of Strathclyde Mathematics Research Report, no.10 (2004).

[9] N. Schopohl and T. J. Sluckin, 1987, Physical Review Letters, 59, pp 2582.

[10] P. Palffy-Muhoray et.al, 1994, Liquid Crystals, 16, pp 713.

[11] I. Dozov and M. Nobili and G. Durand, 1997, Applied Physics Letters, 70, pp 1179.

[12] P.G.De Gennes, The physics of liquid crystals. Oxford, Clarendon Press, 1974.

[13] S. Kralj and E. G. Virga and S. Žumer, 1999, Physical Review E, 60, pp 1858.

[14] S. Kralj and E. G. Virga, 2001, J. Phys. A: Math. Gen.", 34, pp 829.

[15] T. Bellini and M. Buscaglia and C. Chiccoli and F. Mantegazza and P.Pasini and C. Zannoni, 2002, Physical Review Letters, 88, pp 245506.

[16] R. Rosso and E. G. Virga, 1996, J. Phys. A: Math. Gen., 29, pp 4247.

[17] F. Bisi and E.C. Gartland and R. Rosso and E.G. Virga, 2003,

[18] R. Barberi, F. Ciuchi, G. Lombardo, R. Bartolino and G.E. Drand, 2004, Physical Review Letters, 93, pp 137801.

[19] P. Palffy-Muhoray, 2007, Physics Today, 60, pp 54.

[20] C.Tsakonas, A.J. Davidson, C.V.Brown, N.J.Mottram, 2007, Applied Physics Letters, 90, pp 111913.

[21] C.Luo, A.Majumdar and R.Erban, 2012, Physical Review E, 85, pp 061702.

[22] A.Majumdar and A.Zarnescu, 2010, Archive of Rational Mechanics and Analysis, 196, pp 227.

[23] S. Kralj, R. Rosso and E.G. Virga, 2010, Physical Review E, 81, pp 021702.

[24] G.Lombardo et.al, 2012, The European Physical Journal E, 35; pp32.

[25] W.H. Press, B.P. Flannery, S.A. Teukolsky and W.T. Vetterling, Numerical Recipies. Cambridge University Press, Cambridge, 1986.